3D-Bioprinted Phantom with Human Skin Phototypes for Biomedical Optics

Wonjun Yim, Jiajing Zhou, Lekshmi Sasi, Jiayu Zhao, Justin Yeung, Yong Cheng, Zhicheng Jin, Wade Johnson, Ming Xu, Jorge Palma-Chavez, Lei Fu, Baiyan Qi, Maurice Retout, Nisarg J. Shah, Jinhye Bae, and Jesse V. Jokerst*

3D-bioprinted skin-mimicking phantoms with skin colors ranging across the Fitzpatrick scale are reported. These tools can help understand the impact of skin phototypes on biomedical optics. Synthetic melanin nanoparticles of different sizes (70–500 nm) and clusters are fabricated to mimic the optical behavior of melanosome. The absorption coefficient and reduced scattering coefficient of the phantoms are comparable to real human skin. Further the melanin content and distribution in the phantoms versus real human skins are validated via photoacoustic (PA) imaging. The PA signal of the phantom can be improved by: 1) increasing melanin size (3–450-fold), 2) increasing clustering (2–10.5-fold), and 3) increasing concentration (1.3–8-fold). Then, multiple biomedical optics tools (e.g., PA, fluorescence imaging, and photothermal therapy) are used to understand the impact of skin tone on these modalities. These well-defined 3D-bioprinted phantoms may have value in translating biomedical optics and reducing racial bias.

1. Introduction

Human skin offers important physical and immunological protection. It protects against injury, shields radiation, and offers

W. Yim, B. Qi, J. Bae, J. V. Jokerst
Materials Science and Engineering Program
University of California San Diego
La Jolla, CA 92093, USA
E-mail: jjokerst@ucsd.edu

J. Zhou, L. Sasi, J. Zhao, Y. Cheng, Z. Jin, W. Johnson, M. Xu,
J. Palma-Chavez, L. Fu, M. Retout, N. J. Shah, J. Bae, J. V. Jokerst
Department of Nanoengineering
University of California San Diego
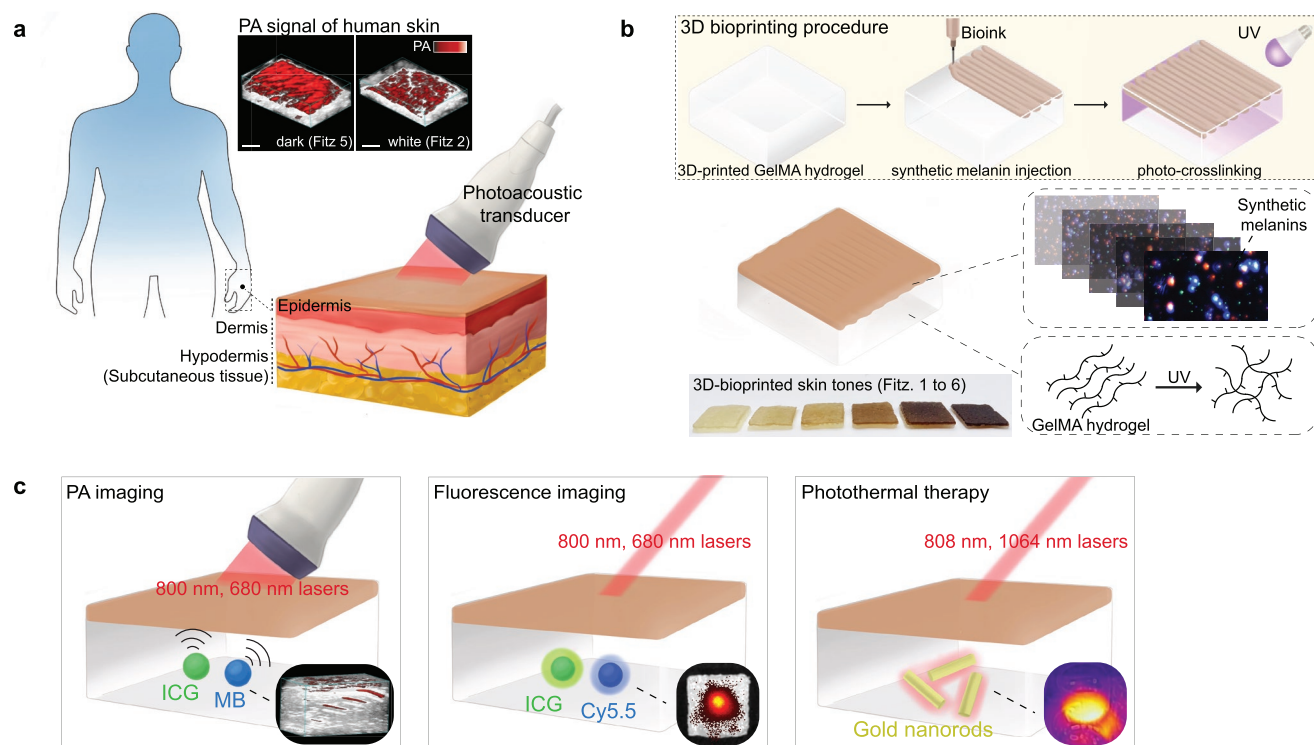La Jolla, CA 92093, USA

J. Yeung
Department of Bioengineering
University of California San Diego
La Jolla, CA 92093, USA

N. J. Shah, J. Bae
Chemical Engineering Program
University of California San Diego
La Jolla, CA 92093, USA

J. V. Jokerst
Department of Radiology
University of California San Diego
La Jolla, CA 92093, USA

antioxidant defense.[1,2] Skin consists of a lamellar structure with diverse cell types (e.g., immune cells, melanocytes, and basal cells) that periodically detach from the basement membrane, move to the surface, and die for self-renewal.[3] Melanocytes are a critical cell type that generate melanin to absorb UV light (290–400 nm), which is a major risk for skin diseases (e.g., melanoma) due to DNA damage.[4–7] Here, melanin-containing organelles called melanosomes are transferred to the surrounding keratinocytes. This increase in melanosome concentration leads to darker skin phototypes, and darker phototypes can be a function of racial background or previous sun exposure, that is, tanning.[8] Indeed, skin pigmentation depends on variations in the size, number, clustering phase, and the proportions between melanin species (e.g., eumelanin and pheomelanin).[9] Skin pigmentation has been quantified using melanosome volume fraction (M_f) parameter: 1.3–6.3% for lightly pigmented adults, 11–16% for moderately pigmented adults, and 18–43% for darkly pigmented adults.[10]

Variations in skin phototypes can complicate biomedical optics. Melanin absorption increases linearly from 800 to 600 nm and exponentially from 600 to 300 nm.[11,12] Darker skin phototypes can absorb and scatter more photons: as a result, incident light is attenuated before it reaches the target of interest, and signal transmission can be impeded back to the sensor. Therefore, variations in skin phototypes have negatively affected many forms of medical optic technology including pulse oximetry,[13,14] cerebral tissue oximeters,[15] optical coherence tomography,[16] wearable electronics,[17–19] photoacoustic (PA) imaging,[20] fluorescence imaging,[21] and photothermal therapy.[22] One recent study compared 48 097 pairs of oxygen saturation levels measured by pulse oximetry and arterial blood gas test obtained from 8675 white patients and 1326 black patients.[13] The results found that pulse oximetry had trouble in diagnosing hypoxemia in 11% Black patients and 3% white patients due to light absorption by melanin.[13,14] Furthermore, wearable electronics (e.g., smartwatches) have reported inaccuracies in heart rate readings occurring more often in users with dark skin than light skin.[17,18] Clearly, the impact of differences in skin phototypes underscore the ongoing need to understand and correct racial bias in optical technologies. While larger

Figure 1. Mimicking human skin phototype for biomedical optics. a) PA transducer imaged melanosomes in human skins of Fitz. 5 and Fitz. 2. The scale bar represents 4 mm. b) The 3D bioprinting procedure to mimic human skin phototypes using synthetic melanin and GelMA hydrogel. The red and blue dots in the inset image are real PDA nanoparticles measured by M-NTA. c) Evaluation of skin tone impact on multiple biomedical optics (e.g., PA imaging, fluorescence imaging, and photothermal therapy). MB, ICG, Cy5.5, and gold nanorods were used to investigate the impact in different wavelengths (680–1064 nm). Insert images describe PA signal, fluorescence, and temperature of the probes under the skin-tone phantoms during the examination.

cohort studies are ideal to define and rectify such bias, tissue-mimicking phantoms that recreate the optical properties of human skin as a function of skin phototypes could offer dramatic time- and cost-savings.[23,24] These phantoms would be attractive to regulatory agencies, device development firms, and patients.

Here, we engineered 3D-bioprinted phantoms with skin phototypes containing synthetic melanin with controllable particle sizes and clustering to mimic the epidermis of different skin phototypes ranging from Fitzpatrick (Fitz) scale 1 to 6.[23,25] The PA signal of human skin changes as a function of melanin absorption:[26,27] the light absorbed by melanin is converted to spatially confined heat that generates acoustic waves.[28–30] This implies that PA can indirectly measure melanosome content and distribution in human skin. Fitz. 5 human cadaver skin showed 3.5-fold higher PA signal than Fitz. 2 human cadaver skin due to higher melanosome content (**Figure 1**a and Figure S1, Supporting Information).

To mimic variable melanosomes in human skin, we studied optical properties and PA signal of synthetic melanin (i.e., polydopamine [PDA]) over: 1) different sizes, 2) mixtures of different sized particles, and 3) clustering phases which are biologically relevant to real melanosomes.[31] Gelatin methacrylate (GelMA)—biomacromolecule gelatin obtained from denatured collagen—was used as a bio-ink (i.e., matrix).[32] 3D bioprinting was then used to fabricate a customized GelMA-based phantom with a thin melanin-containing layer

(i.e., mimicking the epidermal layer in human skin) (Figure 1b). Finally, we quantitatively examined the impact of skin phototypes on PA imaging, fluorescence imaging, and photothermal imaging at different wavelengths (e.g., 680, 800, and 1064 nm) (Figure 1c). Our skin-tone phantom built up by 3D bioprinting is expected to serve as a benchmark calibration tool of light-mediated diagnostics toward clinical use and further underpin development of biomedical optics.

2. Results and Discussion

2.1. Design of Synthetic Melanin

Melanin biogenesis occurs through an oxidation process of tyrosine to dopaquinone by tyrosinase.[33] Melanosomes in human skin vary in terms of size (100–500 nm), shape (e.g., spherical or elliptical), and number of clusters (**Figure 2**a).[9,31] Although the overall structure of melanin remains unclear, the basic structural unit of melanin is a mixed polymer predominantly containing indoles.[33] Melanin from human skin or hair is challenging to obtain because it requires harsh extraction conditions (e.g., strong acids or bases) and multiple purification steps.[34] Thus, PDA was employed here because of its similarity to real melanin in optical absorption, chemical composition, and structure.[35,36] Dopamine can be oxidized into dopamine quinone under basic conditions and further
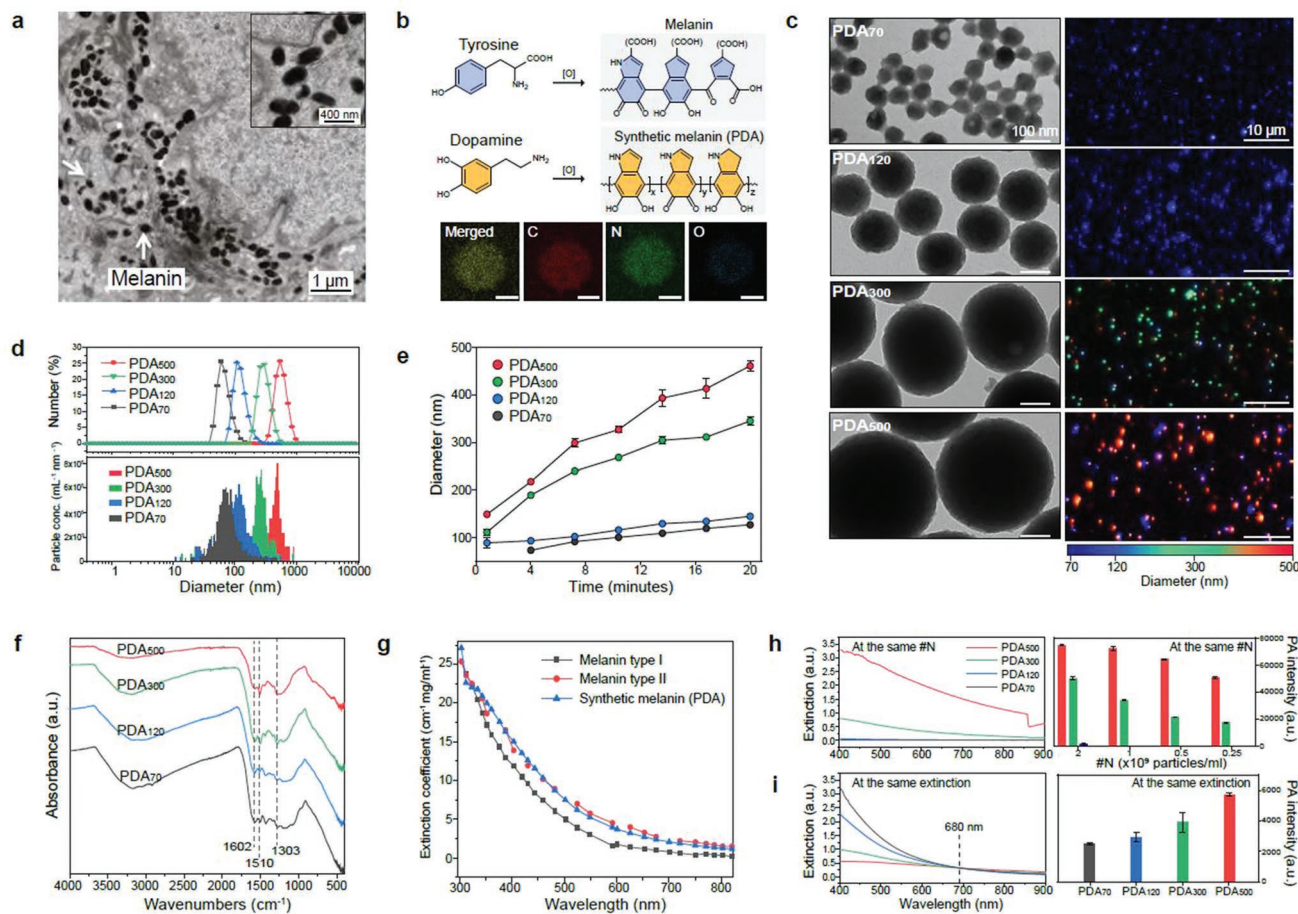
Figure 2. Material characterization of synthetic melanin. a) TEM image of melanin in human skin. b) Chemical structure of melanin and synthetic melanin (PDA). Energy-dispersive X-ray spectroscopy mapping showed that PDA consists of C, N, and O, that is, components of melanin in human skin. The scale bars represent 50 nm. c) TEM (left column) and M-NTA (right column) images of PDAs with different sizes from 70 to 500 nm. Blue (70–150 nm), green (300 nm), and red (>400 nm) dots represent actual PDAs scattered in the water during M-NTA measurements. d) Hydrodynamic diameter confirmed by DLS (top) and M-NTA (bottom). e) Oxidization process of dopamine, showing time-dependent PDA growth. f) FTIR data of PDA nanoparticles. The peaks in PDAs at 1303, 1510, and 1602 cm^{-1} indicate that PDAs consist of the indole structure. g) Extinction coefficients of real and synthetic melanin. Melanin type I and II indicate eumelanin and pheomelanin, respectively. h) Extinction spectra and the corresponding PA signals of different-sized PDAs at the same #N from 0.25 to 2×10^9 particles mL^{-1}. i) Extinction spectra and the corresponding PA signals of different-sized PDAs at the same extinction of 0.3 at 680 nm. The red, green, blue, and black bars in (h), and (i) represent PDA$_{500}$, PDA$_{300}$, PDA$_{120}$, and PDA$_{70}$, respectively. The error bars represent the standard deviation of six regions of interest. The experiment in (h) and (i) was repeated independently three times with similar results. a) Reproduced with permission.[31] Copyright 2018, The Authors. Published by Elsevier, Inc. on behalf of the Society for Investigative Dermatology. g) Data (red circles and black squares) replotted from data published in ref. [40] and ref. [41] and collated at https://omlc. org/spectra/melanin/eumelanin.html.

self-polymerize into indole-rich PDA:[37,38] this structure is widely considered to be a synthetic melanin[36] (Figure 2b). To mimic the variable sizes of melanosomes, we synthesized spherical PDA nanoparticles with different diameters of 70, 120, 300, and 500 nm (referred to as PDA$_{70}$, PDA$_{120}$, PDA$_{300}$, and PDA$_{500}$, respectively) as confirmed by transmission electron microscopy (TEM), scanning electron microscopy (SEM), and multi-laser nanoparticle tracking analysis (M-NTA) (Figure 2c and Figure S2, Supporting Information). The size was adjusted by varying the amount of dopamine feed (2–4 mg mL^{-1}) used for the reaction. The particle size confirmed by M-NTA was consistent with dynamic light scattering (DLS) data, showing that different-sized spherical PDA nanoparticles were uniform and monodispersed (polydispersity index: 0.15 ± 0.02 [PDA$_{70}$],

0.08 ± 0.01 [PDA$_{120}$], 0.03 ± 0.01 [PDA$_{300}$], 0.1 ± 0.02 [PDA$_{500}$]) (Figure 2d and Figure S3, Supporting Information). The formation of PDA nanoparticles occurred under basic condition (pH 12), which induced self-oxidation and polymerization (Figure 2e). Fourier transform infrared (FTIR) spectra data confirmed peaks at 1303, 1510, and 1602 cm^{-1} attributed to the C—N stretching of the indole ring, the C=N of the indole imine, and the C=C of the benzene ring, respectively (Figure 2f).[39]

The extinction coefficient of the synthetic melanin (i.e., PDA$_{70}$) increased from 820 to 300 nm similar to that of real melanin (Figure 2g and Table S1, Supporting Information).[40,41] PDA$_{500}$ showed higher extinction than PDA$_{120}$ at the same number (#N) of nanoparticle due to higher absorption coefficient (μ_a, 97-fold), reduced scattering coefficient (μ_s', 86-fold),

and larger absorption cross-sectional area (18-fold) (Figures S4 and S5, Supporting Information). These observations are consistent with Mie theory and the literature.[42–44] Accordingly, PA signal and spectra of PDA_{500} at the same #N were higher than that of PDA_{70} (450-fold), PDA_{120} (90-fold), and PDA_{300} (3-fold), respectively, because PA signal is a function of optical absorption (Figure 2h and Figures S6 and S7, Supporting Information). In addition to the light absorption, PA signal generation also depends on specific heat capacity, laser fluence, and thermal expansion coefficient.[45] To further study the impact of particle size on PA signal generation, we hold constant extinction values of different-sized PDAs at 680 nm (Figure 2i). Although PDA_{120} had 12.8-fold higher concentration than PDA_{500} at the same extinction (Figure S8 and Movies S1 and S2, Supporting Information), overall μ_s' of different-sized PDAs were similar at 680 nm likely due to the decreased light scattering from the size reduction (Figure S9 and Table S2, Supporting Information).[42,44] Importantly, PDA_{500} still showed higher PA signal and spectra than PDA_{70} (2.3-fold), PDA_{120} (1.9-fold), and PDA_{300} (1.5-fold), respectively, at the same extinction of 0.3 at 680 nm (Figure 2i and Figure S7, Supporting Information). These results indicate that PA signal generation also depends on size-dependent thermal expansion coefficient, and the specific heat capacity (C_p) in which C_p increases with decrease in particle size due to higher thermal vibration energy of surface atoms.[46] In addition, a single PDA_{500} nanoparticle has more surface area to transmit heat to the environment than a single PDA_{120} nanoparticle. In summary, PDA_{500} generated higher PA signal than PDA_{120} both at the same #N (90-fold) and at the same extinction (1.9-fold) due to the large optical absorption (Figure S4, Supporting Information), absorption cross-sectional area (Figure S5, Supporting Information), surface area, and heat capacity.[45,46]

2.2. Cluster-Dependent PA Performance

Melanosomes are individually distributed or form clusters in the human skin.[31] To investigate the function of clusters of melanosomes, various metal ions (Na^+, Mg^{2+}, Fe^{2+}, Ca^{2+}) and other stimuli (NaOH, HCl, sugar, cysteine [Cys]) were applied to make PDA clusters. Metal ions induce PDA clustering because the catechol group in PDA can chelate metal ions, thus forming metal–phenolic networks (Figure S10, Supporting Information).[37,47] The PA signal increased as PDA nanoparticles were clustered as assessed by DLS and inductively coupled plasma-mass-spectrometry (**Figure 3**a and Figure S11, Supporting Information), and there was no background PA signal from Ca^{2+} only (Figure S12, Supporting Information). The highest PA signal was observed in Ca^{2+} which caused significant PDA_{120} aggregation because of its strong binding affinity among the tested metal ions (Figure 3a and Figure S13, Supporting Information).[48] Different Ca^{2+} concentrations ($2–200 \times 10^{-3}$ M) were used to study the relationship between cluster size and PA signal. The results showed that PDA clusters induced by 200×10^{-3} M of Ca^{2+} led to a 1.84-fold higher PA signal than PDA clusters induced by 20×10^{-3} M of Ca^{2+}. There was no increase in PA signal at low Ca^{2+} concentrations (e.g., $2–5 \times 10^{-3}$ M) because this concentration could not induce PDA clusters

(Figure 3b). The formation of PDA clusters significantly decreased the extinction in the range of 400–550 nm while the extinction was increased from 552 to 900 nm likely due to the increased scattering by larger aggregates (Figure 3c and Figure S14, Supporting Information).

We could disassemble PDA clusters via the strong chelating agent ethylenediaminetetraacetic acid (EDTA). After adding EDTA, PDA clusters were entirely disassembled due to the breakdown of metal coordination bonds (Figure S15, Supporting Information). Collectively, the metal chelation was a dominant driving force for PDA clusters.[37] The PA signal of PDA clusters can be activated and deactivated by repeatedly adding EDTA and Ca^{2+} ions over four cycles (Figure 3d and Figure S16, Supporting Information). We explained this increase in PA signal of PDA clusters through two reasons. First, the increased particle size by clustering could have a larger absorption cross-sectional area than small individuals.[31] The ≈1 µm PDA clusters have 579-fold larger cross-sectional area than PDA_{120}. Second, PA signal is a function of thermoelastic expansion that occurs when the surrounding medium is locally heated. The aggregated nanoparticles could cause overlapping thermal fields that improve the rate of heat transfer and amplify PA signal.[28,49]

Human skin involves different-sized melanosomes, and thus we also studied the PA signal of PDA mixtures that contained both PDA_{300} and PDA_{120} at different ratios. The PDA mixture containing 66% of PDA_{300} and 33% of PDA_{120} had 1.8-fold higher PA signal than the PDA mixture containing 33% of PDA_{300} and 66% of PDA_{120} (Figure 3e). In addition, the PA signal of the PDA mixtures further increase by Ca^{2+}-induced PDA clustering. Notably, PDA clusters formed by PDA_{120} exhibited significantly higher (10.5-fold) PA signal than PDA_{120} while the PDA clusters formed by PDA_{300} only increased 1.13-fold, thus indicating that this aggregation-derived PA signal is affected by particle size. To understand the relationship between particle size and aggregation, we used M-NTA to monitor aggregation of PDA mixtures (Figure 3f and Figure S17, Supporting Information). The results showed that PDA_{120} were more prone to aggregate than PDA_{300} because small nanoparticles have a higher surface area-to-volume ratio, which implies a higher surface energy than the large particles (Figure S18, Supporting Information).[50] This explains why PDA_{120} dramatically increased their size (from 120 nm to >1 µm), thus significantly increasing PA signal. In summary, our PA experiments revealed that the PA signal of PDA can be improved by increasing: 1) size (>90-fold: PDA_{500} vs PDA_{120}), 2) clustering ($2–10.5$-fold: 10×10^{-3} M vs 200×10^{-3} M Ca^{2+}), and 3) concentration ($1.3–8$-fold: 1 µg mL^{-1} vs 8 µg mL^{-1} of PDA mixtures).

To use these materials in a phantom, we used a GelMA-based scaffold which can provide 3D supports with characteristics of the native extracellular matrix (Figure S19, Supporting Information). The average thicknesses of dermis and epidermis in human skin are 2.5 and 0.2 mm, respectively,[51] and thus GelMA hydrogel with a thickness of 2.5 mm was first printed to provide the baseline of the epidermis. A PDA-included hydrogel with a thickness of 0.2 mm was then built on the top to mimic human skin phototypes (Movie S3, Supporting Information). The dimension (20 mm × 20 mm × 2.7 mm) of the printed sample was precisely adjustable using 3D-bioprinting. Finally,
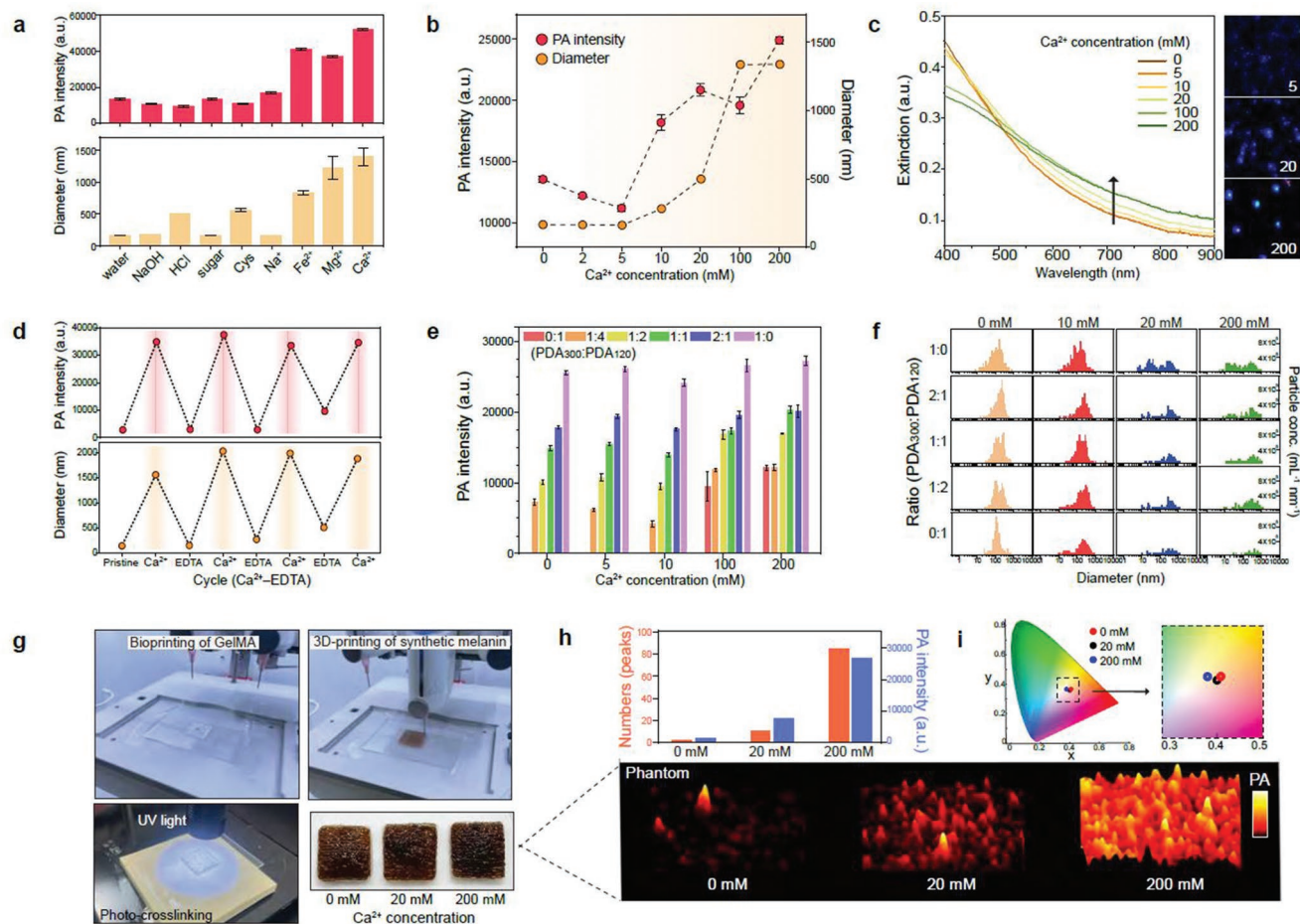
Figure 3. Clusters of synthetic melanin. a) PA signal of PDA clusters. Different metal ions and other sample matrices were used to induce PDA clusters. The error bars represent the standard deviation of six regions-of-interest. b) PA signal of PDA clusters induced by different Ca^{2+} concentrations (from 0 to 200×10^{-3} M). The error bars represent the standard deviation of six regions of interest. c) UV–vis spectra of PDA clusters at different Ca^{2+} concentration. M-NTA image shows higher light scattering (i.e., brighter) of PDA clusters (200×10^{-3} M) than individual PDAs (0×10^{-3} M). The intensity of the blue dots is proportional to light scattering. d) Reversible PA signal upon assembly–disassembly of PDA clusters. PA signal turned "on and off" under repeatedly adding EDTA and Ca^{2+} ions. e) PA signal of PDA mixtures at the same total number of particles. 0:1, 1:4, 1:2, 1:1, 2:1, and 1:0 indicate the particle number ratio of PDA_{300} to PDA_{120}. f) Particle distributions of PDA mixtures at different Ca^{2+} concentrations. g) 3D bioprinting process of skin-tone phantom. The photograph shows the same skin phototype (Fitz. 6) of three-printed phantoms. h) PA signal of 3D-bioprinted phantoms containing PDA mixtures with 0, 20, and 200×10^{-3} M of Ca^{2+} ions. PA signal increased as more PDA clusters led to PA punctuate images. i) CIE coordinates of 3D-printed phantoms containing different amounts of PDA clusters. The experiments in (a), (b), (d), and (h) were repeated independently three times with similar results.

UV light (365 nm) was used to initiate radical polymerization and form covalently crosslinked hydrogels (Figure 3g).

To study the function of PDA clusters when bio-printed, we next prepared three different bio-inks containing clustered PDAs by using 0, 20, and 200×10^{-3} M Ca^{2+}. Each bio-ink had the same total number of PDA_{120} and PDA_{300}. 3D-bioprinted PDA with 200×10^{-3} M of Ca^{2+} showed threefold higher PA signal than PDA with 20×10^{-3} M of Ca^{2+}. There was significantly (>10-fold) higher PA signal than PDA with 0×10^{-3} M of Ca^{2+} similar to the solution phase data in Figure 3e. We also found that the number of PA peaks exponentially increased corresponding to the number of induced PDA clusters: The printed samples with 0, 20, and 200×10^{-3} M of Ca^{2+} showed 2, 11, and 85 of PA peak clusters, respectively (Figure 3h and Figure S20, Supporting Information). In contrast, all three printed samples had the same international commission in illumination (CIE)

coordinates of Fitz. 6 (i.e., skin phototype), thus indicating that skin phototype is more correlated with the number of PDA nanoparticles than the PDA clusters (Figure 3i).

2.3. PA Characterization of Real and Mimicked Human Skin

Melanosomes have been intensively characterized and studied in dermatology.[9,31,52] A recent study measured variable melanosome contents in the different human skin phototypes. It showed that Fitz. 5 human skin contained more and larger melanin than Fitz. 2 human skin; melanin clusters were more often found in Fitz. 2 skin (Figure S21, Supporting Information).[31] To mimic the variable contents of melanosomes, we used PDA mixtures composed of PDA clusters, PDA_{120}, and PDA_{300}. Both real and mimicked human skins had the same
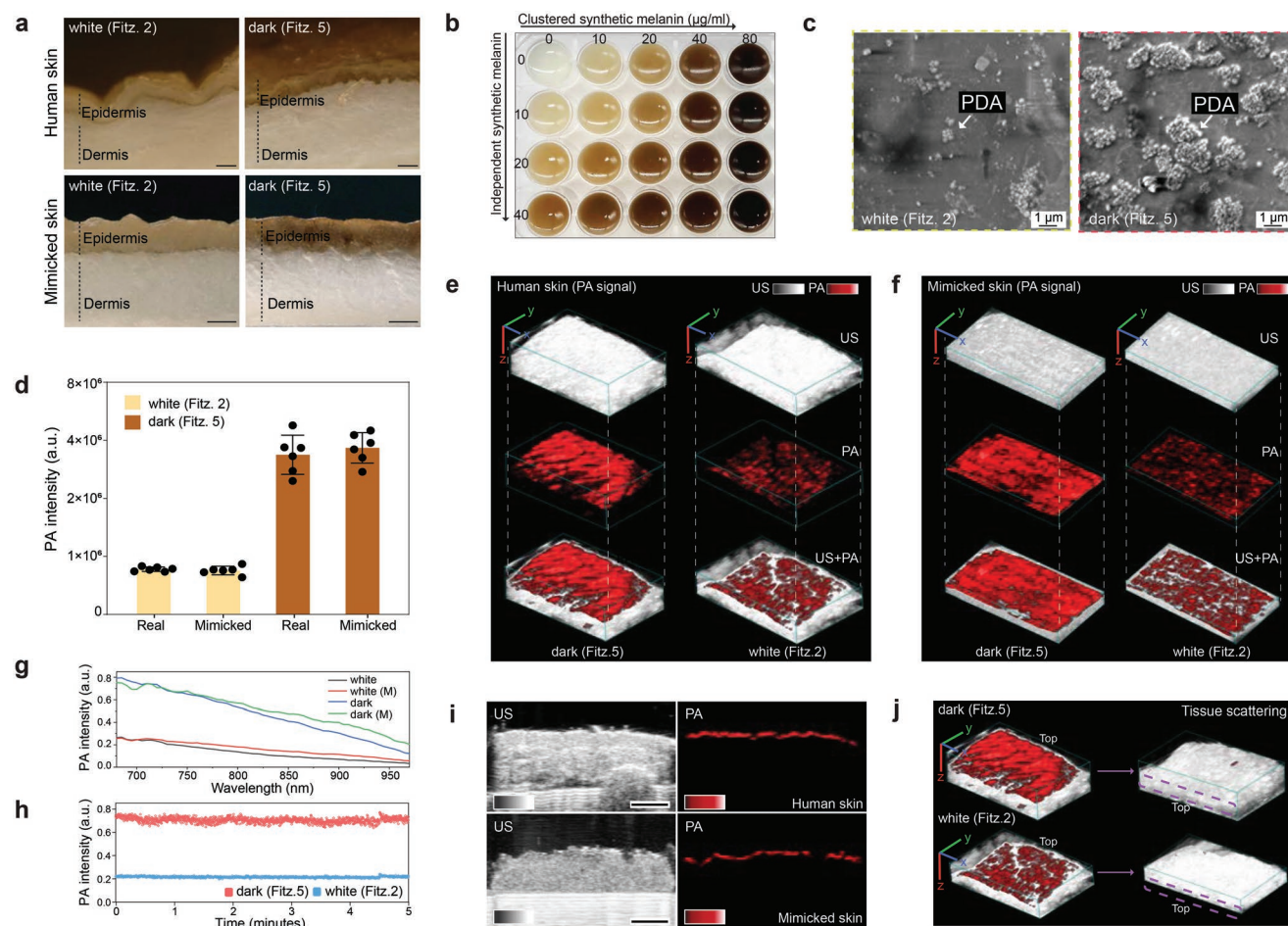
Figure 4. PA comparison between real and mimicked skin. a) Optical images (cross section) of real and mimicked skins. The scale bars represent 0.5 mm. b) Skin phototype variations. Skin colors were readily tunable (From Fitz. 1 to Fitz. 6) by adjusting PDA contents. c) SEM image of PDA mixtures in the printed skin (epidermal layer). d) PA signal comparison between real and mimicked skins. PA signal of mimicked skin was comparable to that of real human skin at the same skin phototype. The error bars represent the standard deviation of six regions of interest. PA and US image of (e) real and (f) mimicked human skins, showing randomly distributed melanosomes in epidermis. The scale bars (x, y, z) represent 4 mm. g) Spectral PA signal from 680 to 970 nm of real and mimicked (M) skins. h) PA signal stability of mimicked skins. i) PA signal of epidermis in real and mimicked skins. The scale bar represents 4 mm. j) Tissue scattering in real human skins. Purple dotted area indicates the region of epidermis after turning the samples upside-down. The scale bars (x, y, z) represent 4 mm. The thicknesses of dermal tissue were 4 mm (Fitz. 5) and 2.7 mm (Fitz. 2). The experiments in (g), (i), and (j) were repeated independently three times with similar results.

thickness of epidermis (about 0.2 mm) and contained melanin with the same color scale (**Figure 4**a and Figure S22, Supporting Information). Different ratios of individual and clustered PDAs were mixed to understand the relationship between PDA contents versus variable skin phototypes. The results showed that skin phototypes are predominantly dependent on the particle concentration (M_f) rather than particle size or PDA clusters (Figure 4b and Figure S23 Supporting Information). As PDA concentration increases (from 1- to 8-fold), PA signal linearly increased from 1.3- to 8-fold, and the color of skin phototype changed from Fitz. 1 to Fitz. 6. In addition, PDA_{120}, PDA_{300}, and PDA clusters were arbitrarily distributed and maintained their spherical shapes in the epidermis of printed skin phantom as confirmed by SEM (Figure 4c).

PA signal of our mimicked skins was matched to that of real human skins: Fitz. 5 skin had 3.5-fold higher PA signal than Fitz. 2 skin in both real and mimicked samples (Figure 4d).

Furthermore, the PA images of real and mimicked skins visualized melanin distribution, indicating that both real and synthetic melanin were randomly distributed; strong PA signal peaks were found where melanosomes were crowded and/or clustered (Figure 4e,f and Figure S24, Supporting Information). Real and mimicked skins showed a comparable PA spectrum from 680 to 970 nm (Figure 4g). The mimicked skin had stable PA signal for 5 min implying stable PDA mixtures under the 680-nm laser illumination (Figure 4h). Ultrasound (US) images revealed 4 mm thickness of human skin composed of the epidermis, dermis, and hypodermis. A strong PA signal was exclusively observed in the basal layer of epidermis where most melanosomes were located (Figure 4i). Likewise, mimicked skins had comparable skin thickness and strong PA signal generated from the epidermis. There was no decrease in sample thickness and PA signal of Fitz. 2 and 5 skin phantoms for 7 days (Figure S25, Supporting Information). Finally,

we inverted the Fitz. 2 and Fitz. 5 human skin samples to investigate tissue scattering in the underlying fat tissue layers of the dermis. No PA signal was observed in the epidermis of either human skin sample due to large light scattering in the dermis. The fat tissue layers in the dermis have low absorption at 680 nm to generate PA signal (Figure 4j and Figure S26, Supporting Information).

2.4. Impact of Skin Phototype on Biomedical Optic Modalities

3D-bioprinted phantoms with skin phototypes from Fitz. 1 to 6 were successfully developed by adjusting the PDA contents used for bio-inks: Fitz. 1, Fitz. 3, and Fitz. 5 contained an M_f of 3%, 12%, and 20%, respectively (Figure S27, Supporting Infor-

mation). The phantom without skin prototype was also fabricated as a negative control (referred to as Fitz. 0). Both the CIE color space and a colorimeter were used to quantify our phantoms with different skin phototypes (Figure S28 and Table S3, Supporting Information). Titanium oxide (TiO$_2$) was also used to mimic tissue scattering in the dermis.[53] We then measured the energy attenuation from 680, 800, and 1064 nm laser beams caused by the mimicked skin phototypes (**Figure 5**a). The results showed that darker skin attenuated more laser energy (mJ) than lighter skin: Fitz. 1, 3, and 5 skin phantoms decreased 1, 3, and 6 mJ energy at 680 nm which is relevant to the absorption peak of deoxyhemoglobin (660 nm).[23] Moreover, the 680-nm laser attenuated 1.3- and 1.98-fold more energy than 800 and 1064 nm lasers, respectively, because of higher light absorption and scattering of synthetic melanin. To further
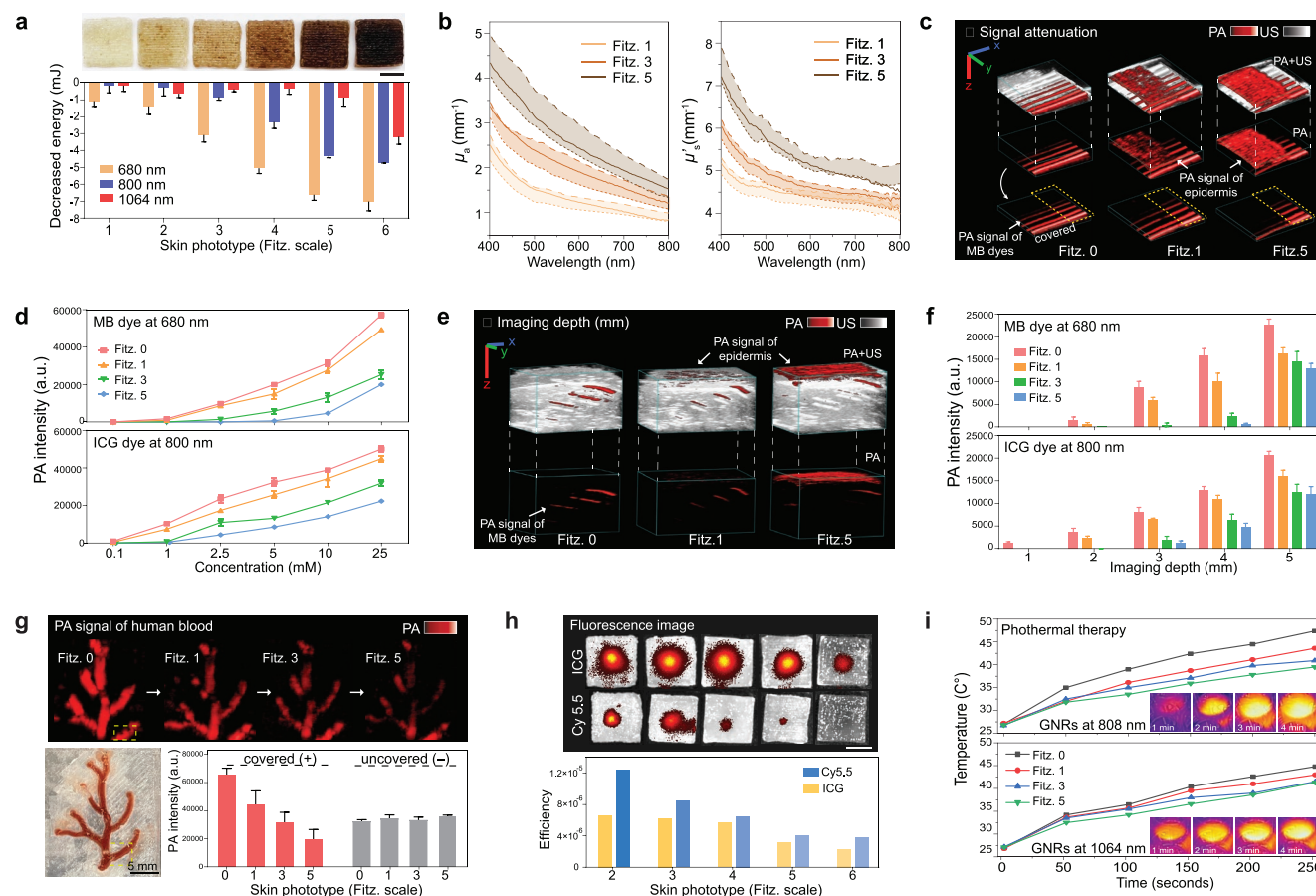
Figure 5. Impact of skin phototypes on biomedical optics. a) Decreased energy of 680, 800, and 1064 nm lasers due to light absorption by mimicked skin phototypes. The error bars represent the standard deviation of three individual samples. Photograph shows 3D-bioprinted skin phantoms with different skin phototypes (from Fitz. 1 to 6). b) μ_a and μ_s' (solid lines) values of Fitz. 1, 3, and 5 skin phantoms. The dotted lines represent the tunable range of μ_a and μ_s' by adjusting PDA content in the epidermis. c) PA image of MB dye covered by Fitz. 1, 3, and 5 skin phantoms. Yellow dotted area remained uncovered showing no decrease in the laser power. The scale bars (x, y, z) represent 4 mm. d) PA signal attenuation of MB and ICG dyes by Fitz. 1, 3, and 5 skin phantoms. The error bars represent the standard deviation of six regions of interests. e) PA image of MB dye in a 5 mm-thick phantom covered by Fitz. 1, 3, and 5 skin phantoms. The scale bars (x, y, z) represent 4 mm. f) PA signal attenuation of MB and ICG dyes at different imaging depths from 1 to 5 mm. MB and ICG dyes (10×10^{-3} M) were covered by Fitz. 1, 3, and 5 skin phantoms. The error bars represent the standard deviation of six regions of interest. g) PA signal attenuation of real human blood. Human blood in the blood vessel scaffold was covered by Fitz. 1, 3, and 5 skin phantoms. The yellow-dotted area remained uncovered as a negative control. The error bar represents the standard deviation of six regions of interest. h) Fluorescence attenuation of Cy5.5 and ICG dye by mimicked skin phototypes. Insert images show that Cy5.5 and ICG dyes were covered by phantoms with different skin phototypes from Fitz. 2 (left) to the Fitz. 5 (right). The scale bar represents 5 mm. i) Impact of skin phototypes on photothermal therapy. NIR-I (808 nm) and NIR-II (1064 nm) lasers were used for the test. Fitz. 0 indicates the phantom without synthetic melanin. The experiments in (a), (d), (f), (g), (h) and (i) were repeated independently three times with similar results.

evaluate this, μ_a and μ_s' of skin-tone phantoms (Fitz. 1, 3, and 5) were characterized using the inverse adding double manual based on reflectance and transmittance measurements of samples in an integrating sphere spectrophotometer (the detailed calculation is described in Supporting Information).[54,55] Both the μ_a and μ_s' of mimicked skin phototypes exponentially increased from 400 to 600 nm and linearly in the 600–900 nm region: The μ_a of Fitz. 5 at 680 nm was 1.37-fold higher than that at 800 nm (Figure 5b). More importantly, μ_a (1.03 mm^{-1}) and μ_s' (4.34 mm^{-1}) values of our mimicked skins were comparable to that of real human skins (μ_a [0.72 ± 0.29 mm^{-1}] and μ_s' [4.89 ± 1.15 mm^{-1}] at 694 nm) (see Table S4, Supporting Information).[12,56] The μ_a and μ_s' of 3D-bioprinted phantoms were tunable by controlling the particle ratio between PDA$_{300}$ and PDA$_{120}$ in the epidermis. For example, the μ_a of the Fitz. 1 skin phantom with 100% of PDA$_{300}$ showed a 1.1-fold higher than that of Fitz. 1 skin phantom with 100% PDA$_{120}$.

We next used these mimicked skin-tone phantoms to study the impact of skin phototypes on biomedical optics technology including PA imaging, fluorescence imaging, and photothermal therapy. For PA imaging, methylene blue (MB) and indocyanine green (ICG) dyes were chosen as contrast agents to demonstrate the utility of the phantom at 680 and 800 nm, respectively. Here, MB and ICG dyes (100 × 10^{-6} M to 25 × 10^{-3} M) were linearly aligned in the tubes and imaged under the Fitz. 1, 3, and 5 skin phantoms (Figure 5c and Figure S29, Supporting Information). The PA signal and spectra of the ICG dye were less compromised by skin phototypes versus MB dye (Figures S30 and S31, Supporting Information). Specifically, MB dye showed 14%, 55%, and 65% PA signal attenuation with Fitz. 1, 3, and 5 skin. ICG showed a 10%, 37%, and 55% decrease in PA signal at the same dye concentration (Figure 5d). Samples in the yellow dotted area in Figure 5c were intentionally uncovered to show that there was no decrease in laser power and/or photobleaching of the dye during the measurement. We further studied the imaging depth of MB and ICG dye with the phantoms. The 5 mm-thick GelMA phantom including TiO$_2$ (0.5 mg mL^{-1}) was 3D-printed, and each sample was injected at heights 1 mm apart (Figure 5e and Figure S32, Supporting Information). The Fitz. 5 skin phantom has PA signal of MB dye that was attenuated by 44%, 97%, and 100% at depths of 1, 2, and 3 mm, respectively. The PA signal of the ICG dye was decreased by 43%, 63%, and 85% of PA signals at the same depths (Figure 5f). These results indicated that ICG dye had higher imaging depth due to its longer absorption wavelength (800 nm). In this NIR region, melanin has lower light absorption and scattering. We further designed a blood vessel scaffold to measure the PA signal of real human blood under different skin phototypes to investigate the impact of imaging deoxyhemoglobin (Figure S33, Supporting Information). PA images showed that 33%, 52%, and 70% of PA signals decreased under the Fitz. 1, 3, and 5 skin phantoms. There was a yellow dotted area that remained uncovered. This showed no decrease in laser power or sample degradation (Figure 5g).

Fluorescence could also be affected by melanin. Thus, cyanine5.5 (Cy5.5) and ICG dyes at the same dye concentration (100 × 10^{-6} M) were used to evaluate the impact of skin phototypes on their corresponding excitation (i.e., 680 and 800 nm, respectively). Not surprisingly, Cy5.5 signal decreased by 32%

and 69% under the Fitz. 3 and 5 phantoms, respectively; the ICG dye only decreased by 6% and 53%, thus confirming the wavelength-dependent fluorescence attenuation (Figure 5h). Photothermal therapy also often uses near-infrared (NIR) light. Here, gold nanorods (GNRs) with two different aspect ratios (e.g., 3.3 and 7.3) were synthesized and had a longitudinal absorption peak at 800 and 1062 nm, respectively (Figure S34, Supporting Information). Two different NIR lasers (i.e., 808 and 1064 nm) were used to irradiate GNRs at an O.D. (= 1) underneath different skin phantoms. A thermal camera was used to record the temperature (Figure 5i). The results revealed that the temperature increase facilitated by the GNRs decreased as a function of phototype: Fitz. 1 (8%), Fitz. 3 (14%), and Fitz. 5 (17%) versus Fitz. 0 when irradiated by the 808 nm laser. GNRs irradiated by 1064 nm exhibited relatively minor decreases in temperature: Fitz. 1 (4%), Fitz. 3 (7%), and Fitz. 5 (8%). The 1064 nm (second NIR [NIR-II]) laser was significantly less influenced by skin phototypes.

3. Conclusions

Phantom-based testing is a powerful approach to evaluate the performance of various optical devices and judge quality of medical imaging without risks to human. Skin-mimicking acellular phantoms have been developed for biomedical optics.[23,57–60] One phantom used gelatin and synthetic melanin to make 0.1 mm-thick epidermal layer and characterized tunable mechanical, optical, and acoustic properties.[57] However, this hydrogel-based phantom is limited to control the thickness of each layer and needs vacuum sealed container for storage. In other study, poly(dimethylsiloxane) (PDMS) silicone and ground coffee were used to make tissue-mimicking phantom.[60] Although PDMS-based phantom provides high stability and simplicity, ground coffee is limited to mimic optical absorption of real human skin. To improve this, one recent study used synthetic melanin with PDMS and showed high stability with comparable absorption values to real human skin.[23] However, synthetic melanin used in the previous studies[23,57,59,60] is a form of solid powder (i.e., small molecule) which lacks bio-relevant size and shape to real melanosomes. All the phantoms used different powder concentrations to achieve different skin pigmentation levels which could lose scattering component of real melanosomes. Furthermore, they have not validated the impact of skin tones on biomedical imaging equipment.

Here we developed skin-mimicking phantoms with synthetic melanin (i.e., PDA) as a tool to quantify the impact of skin phototypes on multiple biomedical optics (e.g., PA, photothermal, and fluorescence imaging). To mimic optical properties of melanin, we investigated the light absorption of spherical PDAs in different sizes, mixtures, and clustering phases. Our skin phantoms are enabled by 3D bioprinting, which provides precise deposition of biomaterials, high controllability, good reproducibility, and low cost compared to mold-based phantom fabrications.[61] Human skin consists of multiple thin layers with different thicknesses (0.1–5 mm) and materials, indicating that bioprinting could provide a better platform to mimic the human skin.[61–63] 3D bioprinting also offers customized phantom designs for testing various target of interests

(e.g., imaging depth and blood vessel) for medical imaging devices. GelMA-based scaffolds could serve as extracellular matrix for cell growth, providing more opportunities for deciphering the role of melanin in cell regeneration against UV-light as a future study.[62,64] Our skin phantoms will provide quantitative data of skin tone impact for other biomedical optics (e.g., pulse oximeter and wearables) to deliver more accurate and objective assessments of the device performance. Finally, our methods possibly motivate more phantom studies and will improve device instrumentation and algorithms to correct for race-based bias in biomedical optics.

4. Experimental Section

Synthesis of GelMA Hydrogel: Briefly, gelatin from a porcine skin was fully dissolved in PBS (10% w/v) at 55 °C, and then methacrylic anhydride was added dropwise (0.5 mL min^{-1}) until the target volume reached.[32] For the methacrylation reaction, the mixture was vigorously stirred at 1000 rpm for 2 h. The solution was then centrifuged at 1000g for 2 min to remove excess methacrylic anhydride. Supernatants were diluted five times with additional PBS to stop the reaction followed by dialysis against distilled water (12–14 kDa cut-off, refreshed water five times) for 5 days at 40 °C. Unreacted methacrylic anhydride and salts were further removed during the dialysis. The GelMA hydrogel was placed at −80 °C overnight and lyophilized for 5 days, thus forming a porous white foam. The product was stored at −80 °C for future use (Figure S35, Supporting Information).

Synthesis of Synthetic Melanin: Briefly, 5 mL of distilled water and 2 mL of ethanol were mixed under vigorous stirring at room temperature followed by addition of 500 µL of fresh dopamine solution (40 mg mL^{-1} in distilled water).[35] Then, 100 µL of ammonium hydroxide solution was added to trigger the polymerization. The color immediately changed from yellow to dark brown within 20 min. The solution was stirred at 900 rpm overnight. The size of the PDA could be readily controlled by adjusting the amount of dopamine. For example, 500, 600, 700, and 800 µL of dopamine solution forms PDA with sizes of 70, 120, 300, and 500, respectively. The samples were purified with centrifugation at 14 000g (for PDA$_{70}$), 7000g (for PDA$_{120}$), 2000g (for PDA$_{300}$), and 1000g (for PDA$_{500}$) for 10 min. The pellet was redispersed in water for future use.

Bio-Ink Preparation and Bio-Printing Procedure: Briefly, freeze-dried GelMA macromers were dissolved in PBS (10% w/v) at 50 °C for 20 min followed by adding alginic acid (4% w/v) and photoinitiator (0.5% w/v).[65] During bio-ink preparation, the sample was covered by aluminum foil (to prevent photo-crosslink from the light) and gently mixed for 1 h. Synthetic melanin was added in GelMA macromer before adding the photoinitiator. Different skin phototypes were readily tunable by adjusting different amounts of synthetic melanin in GelMA macromer. For example, 4, 8, 12, 16, 20, and 30 µL of PDA mixtures (0.01 mg mL^{-1}) that contain 20% of PDA clusters, 30% of PDA$_{120}$, and 50% of PDA$_{300}$ were mixed with 1 mL of GelMA macromer to prepare bio-inks for different skin phototypes from Fitz. 1 (4 µL) to Fitz. 6 (30 µL). In addition, the 10–100 µL of PDA mixtures were deposited on the interface between the epidermis and the dermis to mimic basal layers (the innermost layer of the epidermis) where most of melanin resides. The prepared bio-inks were then stored at 4 °C and warmed at 37 °C for 30 min before use. The 3D-bioprinting procedure was performed using a BioX 3D bioprinter (CELLINK+). Printing parameters (e.g., temperature, pressure, and speed) influenced the printing quality and distribution of synthetic melanin. First, printing temperature was controlled at room temperature (25 °C) where bio-ink maintained its gel-like viscosity. Second, printing pressure was correlated with diameter of needle and printing speed. Notably, different-sized needle (e.g., diameter and length) required different printing pressure and speed. In this study, gauge size and length of needle were 20 G and length 0.25 inch. Printing pressure was controlled at 20–70 kPa pressure. Otherwise, high

pressure (>150 kPa) extruded bio-ink irregularly. Last, printing speed was controlled at 1.5–2.5 mm s^{-1}. After bioprinting, 365 nm of UV light with an intensity of 25 mW cm^{-2} was used to trigger photo-crosslinking for 5 min. Specifically, good bioprinting quality could be achieved by careful selections of the needle (e.g., gauge [20G]), printing speed (2 mm s^{-1}), pressure (25 kPa), temperature (25 °C), as well as the rheology of the bio-ink. The printed skin phantoms were then stored in a petri dish sealed with parafilm covered by aluminum foil for future use.

Photoacoustic Imaging of Human Skin Specimens: All work with human subjects was done in accordance with institutional review board guidelines and approval (project #191998X). Two human skin tissues (15 cm × 15 cm, white and dark) were donated from UCSD and UCI Health Centers. Whole human blood was collected from a healthy donor following guidelines. Informed consent of all participants was obtained prior to the experiment. Human skin samples were stored in −80 °C. Prior to the experiments, the skin was thawed at the room temperature and razor blades were used to cut the skin specimens with the size of 2 cm × 2 cm. The specimens were immersed in the formalin fixation buffer overnight. PA imaging was acquired using a Vevo 2100 LAZR (Visual Sonic, USA), with a 21 MHz transducer (LZ-250). Laser intensity was optimized and calibrated. Ex vivo human skin specimens were cleaned three times with deionized water before and after the PA measurements.

Supporting Information

Supporting Information is available from the Wiley Online Library or from the author.

Conflict of Interest

The authors declare no conflict of interest.

Author Contributions

W.Y. and J.V.J. conceived the idea and designed the materials and method for skin phototypes-mimicked phantoms. W.Y. conducted the major material synthesis and experimental works. J.Z., L.S., J.Z., and J.B. helped with 3D-bioprinting experiments. J.Y., Y.C., Z.J., M.X., L.F., B.Q., and M.R. assisted with material design and characterizations. W.J. and N.J.S. helped with fluorescence experiments. W.Y. and J.V.J. analyzed the result and wrote the manuscript with input from all authors.

Data Availability Statement

The data that support the findings of this study are available from the corresponding author upon reasonable request.

[1] B. Dyring-Andersen, M. B. Løvendorf, F. Coscia, A. Santos, L. B. P. Møller, A. R. ColaçO, L. Niu, M. Bzorek, S. Doll, J. L Andersen, R. A. Clark, L. Skov, M. B. M. Teunissen, M. Mann, *Nat. Commun.* **2020**, *11*, 5587.

[2] V. T. Natarajan, P. Ganju, A. Ramkumar, R. Grover, R. S. Gokhale, *Nat. Chem. Biol.* **2014**, *10*, 542.

[3] T. Lechler, E. Fuchs, *Nature* **2005**, *437*, 275.

[4] G. T. Bowden, *Nat. Rev. Cancer* **2004**, *4*, 23.

[5] T. Bald, T. Quast, J. Landsberg, M. Rogava, N. Glodde, D. Lopez-Ramos, J. Kohlmeyer, S. Riesenberg, D. Van Den Boorn-Konijnenberg, R. Reuten, B. Schadow, H. Weighardt, D. Wenzel, I. Helfrich, D. Schadendorf, W. Bloch, M. E. Bianchi, C. Lugassy, R. L. Barnhill, M. Koch, B. K. Fleischmann, W. Kolanus, E. Gaffal, *Nature* **2014**, *507*, 109.

[6] J. H. Epstein, *J. Am. Acad. Dermatol.* **1983**, *9*, 487.

[7] M. S. Eller, M. Yaar, B. A. Gilchrest, *Nature* **1994**, *372*, 413.

[8] N. L. Wicks, J. W. Chan, J. A. Najera, J. M. Ciriello, E. Oancea, *Curr. Biol.* **2011**, *21*, 1906.

[9] H.-Y. Thong, S.-H. Jee, C.-C. Sun, R. E. Boissy, *Br. J. Dermatol.* **2003**, *149*, 498.

[10] S. L. Jacques, *Adv. Opt. Imaging. Photon. Migr.* **1996**, *2*, 364.

[11] H. Ou-Yang, G. Stamatas, N. Kollias, *J. Invest. Dermatol.* **2004**, *122*, 492.

[12] S. L. Jacques, *Phys. Med. Biol.* **2013**, *58*, R37.

[13] M. W. Sjoding, R. P. Dickson, T. J. Iwashyna, S. E. Gay, T. S. Valley, *N. Engl. J. Med.* **2020**, *383*, 2477.

[14] E. R. Gottlieb, J. Ziegler, K. Morley, B. Rush, L. A. Celi, *JAMA Intern. Med.* **2022**, *182*, 849.

[15] P. E. Bickler, J. R. Feiner, M. D. Rollins, *Anesth. Analg.* **2013**, *117*, 813.

[16] J. K. O'Rese, C. A. Girkin, D. L. Budenz, M. K. Durbin, W. J. Feuer, *Arch. Ophthalmol.* **2012**, *130*, 312.

[17] B. Bent, B. A. Goldstein, W. A. Kibbe, J. P. Dunn, *npj Digital. Med.* **2020**, *3*, 18.

[18] I. Ray, D. Liaqat, M. Gabel, E. de Lara, in *2021 IEEE Int. Conf. on Pervasive Computing and Communications Workshops and other Affiliated Events (PerCom Workshops)*, IEEE, Piscataway, NJ, USA **2021**, pp. 213–219.

[19] P. J. Colvonen, P. N. DeYoung, N.-O. A. Bosompra, R. L. Owens, *Sleep* **2020**, *43*, zsaa159.

[20] X. Li, U. S. Dinish, J. Aguirre, R. Bi, K. Dev, A. B. E. Attia, S. Nitkunanantharajah, Q. H. Lim, M. Schwarz, Y. W. Yew, S. T. G. Thng, V. Ntziachristos, M. Olivo, *J. Biophotonics.* **2019**, *12*, e201800442.

[21] M. Y. Rennie, D. Dunham, L. L. Teene, R. Raizman, R. Hill, R. Linden, *Diagnostics* **2019**, *9*, 22.

[22] J. Joensen, J. H. Demmink, M. I. Johnson, V. V. Iversen, J. M. Bjordal, *Photomed. Laser Surg.* **2011**, *29*, 145.

[23] A. Afshari, R. B. Saager, D. Burgos, W. C. Vogt, J. Wang, G. Mendoza, S. Weininger, K.-B. Sung, A. J. Durkin, T. J. Pfefer, *Biomed. Opt. Express* **2022**, *13*, 2909.

[24] R. B. Saager, A. Quach, R. A. Rowland, M. L. Baldado, A. J. Durkin, *J. Biomed. Opt.* **2016**, *21*, 067001.

[25] W. E. Roberts, *Dermatol. Clin.* **2009**, *27*, 529.

[26] Y. Mantri, J. V. Jokerst, *Biomed. Opt. Express* **2022**, *13*, 875.

[27] R. Chen, S. Huang, T. Lin, H. Ma, W. Shan, F. Duan, J. Lv, J. Zhang, L. Ren, L. Nie, *Nat. Nanotechnol.* **2021**, *16*, 455.

[28] W. Yim, K. Takemura, J. Zhou, J. Zhou, Z. Jin, R. M. Borum, M. Xu, Y. Cheng, T. He, W. Penny, B. R. Miller III, J. V. Jokerst, *ACS Nano* **2021**, *16*, 683.

[29] Z. Wu, F. Duan, J. Zhang, S. Li, H. Ma, L. Nie, *Biomed. Opt. Express* **2019**, *10*, 3425.

[30] Q. Yu, S. Huang, Z. Wu, J. Zheng, X. Chen, L. Nie, *J. Nucl. Med.* **2020**, *61*, 1079.

[31] I. Hurbain, M. Romao, P. Sextius, E. Bourreau, C. Marchal, F. Bernerd, C. Duval, G. A. Raposo, *J. Invest. Dermatol.* **2018**, *138*, 647.

[32] J. W. Nichol, S. T. Koshy, H. Bae, C. M. Hwang, S. Yamanlar, A. Khademhosseini, *Biomaterials* **2010**, *31*, 5536.

[33] P. A. Riley, *Int. J. Biochem. Cell Biol.* **1997**, *29*, 1235.

[34] I.-E. Pralea, R.-C. Moldovan, A.-M. Petrache, M. Moldovan, M. Ene, M. Radu, C.-A. Iuga, *Int. J. Mol. Sci.* **2019**, *20*, 3943.

[35] H. Lee, S. M. Dellatore, W. M. Miller, P. B. Messersmith, *Science* **2007**, *318*, 426.

[36] C. Battistella, N. C. Mccallum, K. Gnanasekaran, X. Zhou, V. Caponetti, M. Montalti, N. C. Gianneschi, *ACS Cent. Sci.* **2020**, *6*, 1179.

[37] D. Wu, J. Zhou, M. N. Creyer, W. Yim, Z. Chen, P. B. Messersmith, J. V. Jokerst, *Chem. Soc. Rev.* **2021**, *50*, 4432.

[38] W. Yim, J. Zhou, Y. Mantri, M. N. Creyer, C. A. Moore, J. V. Jokerst, *ACS Appl. Mater. Interfaces* **2021**, *13*, 14974.

[39] K. Patel, N. Singh, J. Yadav, J. M. Nayak, S. K. Sahoo, J. Lata, D. Chand, S. Kumar, R. Kumar, *Phys. Chem. Chem. Phys.* **2018**, *20*, 5744.

[40] P. R. Crippa, V. Cristofoletti, N. Romeo, *Biochim. Biophys. Acta, Gen. Subj.* **1978**, *538*, 164.

[41] T. Sarna, R. C. Sealy, *Photochem. Photobiol.* **1984**, *39*, 69.

[42] Q. Fu, W. Sun, *Appl. Opt.* **2001**, *40*, 1354.

[43] J. Shang, X. Gao, *Chem. Soc. Rev.* **2014**, *43*, 7267.

[44] Y. Pu, J. Chen, W. Wang, R. R. Alfano, in *Neurophotonics and Biomedical Spectroscopy*, Elsevier, New York **2019**, pp. 229–252.

[45] Y. Mantri, J. V. Jokerst, *ACS Nano* **2020**, *14*, 9408.

[46] B.-X. Wang, L.-P. Zhou, X.-F. Peng, *Int. J. Thermophys.* **2006**, *27*, 139.

[47] H. Ejima, J. J. Richardson, K. Liang, J. P. Best, M. P. Koeverden, G. K. Such, J. Cui, F. Caruso, *Science* **2013**, *341*, 154.

[48] Z. Fan, L. Sun, Y. Huang, Y. Wang, M. Zhang, *Nat. Nanotechnol.* **2016**, *11*, 388.

[49] C. L. Bayer, S. Y. Nam, Y.-S. Chen, S. Y. Emelianov, *J. Biomed. Opt.* **2013**, *18*, 016001.

[50] W. Zhang, in *Nanomaterial* (Eds: D. G. Capco, Y. Chen), Springer, New York **2014**, pp. 19–43.

[51] M. C. Branchet, S. Boisnic, C. Frances, A. M. Robert, *Gerontology* **1990**, *36*, 28.

[52] R. E. Boissy, *Exp. Dermatol.* **2003**, *12*, 5.

[53] A. Hariri, J. Palma-Chavez, K. A. Wear, T. J. Pfefer, J. V. Jokerst, W. C. Vogt, *J. Photoacoust.* **2021**, *22*, 100245.

[54] S. A. Prahl, M. J. C. Van Gemert, A. J. Welch, *Appl. Opt.* **1993**, *32*, 559.

[55] S. A. Prahl, in *Optical-Thermal Response of Laser-Irradiated Tissue* (Ed: A. J. Welch, M. J. C. Gemert), Springer, New York **1995** pp. 101–129.

[56] Y. Shimojo, T. Nishimura, H. Hazama, T. Ozawa, K. Awazu, *J. Biomed. Opt.* **2020**, *25*, 045002.

[57] A. I. Chen, M. L. Balter, M. I. Chen, D. Gross, S. K. Alam, T. J. Maguire, M. L. Yarmush, *Med. Phys.* **2016**, *43*, 3117.

[58] R. B. Saager, D. J. Cuccia, A. J. Durkin, *J. Biomed. Opt.* **2010**, *15*, 017012.

[59] O. O. Soyemi, M. R. Landry, Y. Yang, P. O. Idwasi, B. R. Soller, *Appl. Spectrosc.* **2005**, *59*, 237.

**ADVANCED
SCIENCE NEWS**

www.advancedsciencenews.com

**ADVANCED
MATERIALS**

www.advmat.de

[60] R. B. Saager, C. Kondru, K. Au, K. Sry, F. Ayers, A. J. Durkin, *Proc. SPIE* **2010**, *7567*, 756706.

[61] H.-W. Kang, S. J. Lee, I. K. Ko, C. Kengla, J. J. Yoo, A. Atala, *Nat. Biotechnol.* **2016**, *34*, 312.

[62] Y. Huyan, Q. Lian, T. Zhao, D. Li, J. He, *Int. J. Bioprint.* **2020**, *6*, 246.

[63] W. L. Ng, J. T. Z. Qi, W. Y. Yeong, M. W. Naing, *Biofabrication* **2018**, *10*, 025005.

[64] J. C. Yang, J. Mun, S. Y. Kwon, S. Park, Z. Bao, S. Park, *Adv. Mater.* **2019**, *31*, 1904765.

[65] N. R. Barros, H.-J. Kim, M. J. Gouidie, K. Lee, P. Bandaru, E. A. Banton, E. Sarikhani, W. Sun, S. Zhang, H.-J. Cho, M. C. Hartel, S. Ostrovidov, S. Ahadian, S. M. Hussain, N. Ashammakhi, M. R. Dokmeci, R. D. Herculano, J. Lee, A. Khademhosseini, *Biofabrication* **2021**, *13*, 035030.